

Efficient optimization of variational tensor-network approach to three-dimensional statistical systems

Xia-Ze Xu,^{1,*} Tong-Yu Lin,^{1,*} and Guang-Ming Zhang^{2,3,†}

¹*State Key Laboratory of Low Dimensional Quantum Physics and
Department of Physics, Tsinghua University, Beijing 100084, China*

²*School of Physical Science and Technology, ShanghaiTech University, Shanghai 201210, China*

³*Department of Physics, Tsinghua University, Beijing 100084, China*

(Dated: June 25, 2025)

Variational tensor network optimization has become a powerful tool for studying classical statistical models in two dimensions. However, its application to three-dimensional systems remains limited, primarily due to the high computational cost associated with evaluating the free energy density and its gradient. This process requires contracting a triple-layer tensor network composed of a projected entangled pair operator and projected entangled pair states. In this paper, we employ a split corner-transfer renormalization group scheme tailored for the contraction of such triple-layer networks, which reduces the computational complexity from $\mathcal{O}(D^{12})$ in conventional methods to $\mathcal{O}(D^9)$. Through numerical benchmarks on the three-dimensional classical Ising model, we demonstrate that the proposed scheme achieves numerical results comparable to the most recent Monte Carlo simulations, while also providing a substantial speedup over previous variational tensor network approaches. This makes this method well-suited for efficient gradient-based optimization in three-dimensional tensor network simulations.

I. INTRODUCTION

The study of statistical models significantly deepens our understanding of collective phenomena and phase transitions. However, exactly solvable models remain rare, leading contemporary research to rely increasingly on numerical methods such as Monte Carlo simulations [1–3] and the conformal bootstrap [4–6]. In last decades, tensor networks have emerged as a powerful numerical framework for studying statistical models. In this approach, the partition function is represented as a tensor network and then approximately contracted. For two-dimensional (2D) statistical models, tensor network methods are well-established, with techniques like the imaginary time evolution [7, 8], the tensor renormalization group (TRG) [9–12], the corner transfer matrix renormalization group (CTMRG) [13], and the gradient-based variational method demonstrating both high efficacy and accuracy [14–16]. These methods have proven efficient in addressing a broad range of problems, including spin models with both discrete and continuous degrees of freedom [17–19], as well as both non-frustrated and frustrated spin systems [20–22].

In contrast, tensor network methods for three-dimensional (3D) statistical models remain less explored. The primary computational bottleneck arises from the high cost of contracting 3D networks. For example, in the gradient-based variational scheme, the partition function problem is reformulated as a leading eigenvalue problem for a transfer matrix expressed in the form of a projected entangled-pair operator (PEPO) and its leading eigenvector represented by a projected entangled-pair state

(PEPS). The optimization of PEPS and the calculation of physical quantities require contracting a triple-layer tensor network of PEPS and PEPO with a bond dimension of $\mathcal{O}(D^2d)$, where D and d represent the bond dimensions of PEPS and PEPO, respectively, which is computationally expensive. Earlier attempts to use variational methods also encountered problems related to numerical instability during optimization [23–26]. To the best of our knowledge, variational approaches for 3D partition functions have been limited to small bond dimensions ($D = 2 - 4$) [27, 28], which is lack of accuracy of the calculation results. The generalization of other methods to three dimensions also encounters challenges. For instance, a direct generalization of the CTMRG method suffers from the extremely high order of bond dimension in computational complexity and the slow decay of the spectrum of the density matrices constructed by corner-transfer tensors [29, 30]. Additionally, extending the tensor renormalization group (TRG) method to three dimensions faces challenging due to the increase in computational complexity with bond dimension and the change in lattice topology during renormalization [12].

To address the challenge of contracting tensor networks in high dimensions, various methods have been proposed to reduce the computational cost [12, 31, 32]. One promising method is the nesting technique, first introduced in the context of calculating physical quantities in 2D quantum systems [33] and later adapted for calculating physical quantities in 3D classical systems [34]. This technique compresses the double-layer tensor network into a single layer, which is then contracted using the standard multi-site CTMRG algorithm. Recently, this method was further adapted for gradient-based variational infinite PEPS (iPEPS) optimization in 2D quantum systems using a carefully designed split-CTMRG scheme [35, 36].

* These authors contributed equally.

† zhanggm@shanghaitech.edu.cn

In this work, we extend the nesting idea and split-CTMRG method to variational iPEPS optimization for 3D classical statistical models. Unlike quantum systems with local Hamiltonians, the 3D case requires contracting both double- and triple-layer networks. We propose a split corner transfer matrix (split-CTM) environment for triple-layer networks and an accompanying renormalization group scheme. Our approach surpasses traditional methods in efficiency, enabling variational optimization of iPEPS with larger bond dimensions.

The paper is organized as follows. In section II, we show the basic idea of variational iPEPS optimization of 3D classical model and the computation bottleneck for tradition method. In section III, the triple-layer split-CTMRG scheme is explained in detail. In section IV, we take the 3D Ising model as a benchmark to show the performance of this new scheme. Finally, in section V, we discuss potential improvements and generalizations of the algorithm.

II. VARIATIONAL IPEPS METHOD FOR 3D CLASSICAL STATISTICAL MODEL

We begin by reviewing the gradient-based iPEPS optimization method [27, 37, 38]. To implement the tensor network method, the first step is to represent the partition function of the statistical model as a tensor network. As an example, consider classical spin models with nearest-neighbor interactions on a cubic lattice with the Hamiltonian given by

$$H = \sum_{\langle i,j \rangle} h(s_i, s_j), \quad (1)$$

where $\langle i, j \rangle$ refers to nearest neighbors, and s_i denotes the spin variables. The partition function can be decomposed into a tensor network, expressed as the product of local Boltzmann weights on the lattice links

$$\mathbb{Z} = \sum_{\{s_i\}} \prod_{\langle i,j \rangle} e^{-\beta h(s_i, s_j)} = \sum_{\{s_i\}} \prod_{\langle i,j \rangle} W(s_i, s_j). \quad (2)$$

This equation can be transformed into a tensor network, as shown in Fig. 1(a), where the δ tensor on the lattice sites is defined by

$$\delta(s_1, s_2, s_3, s_4, s_5, s_6) = \begin{cases} 1 & s_1 = s_2 = s_3 = s_4 = s_5 = s_6 \\ 0 & \text{other cases} \end{cases} \quad (3)$$

This ensures that all indices of W take the same value at the joint point.

To further transform the tensor network into a uniform one, we split the matrix W by using singular value decomposition

$$\begin{aligned} W_l(s_i, s_j) &= \sum_{s_k} \left(U\sqrt{S} \right) (s_i, s_k) \left(\sqrt{S}V \right) (s_k, s_j) \\ &= \sum_{s_k} \sqrt{W}(s_i, s_k) \sqrt{W}(s_k, s_j) \end{aligned} \quad (4)$$

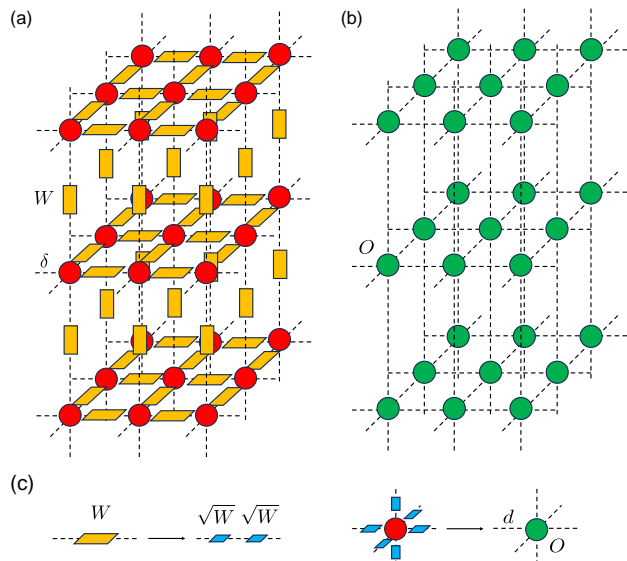


FIG. 1. Tensor network representation of the partition function for the 3D classical model. (a) The tensor network (TN) representation, consisting of a δ tensor on each site and a W matrix on each link. (b) The TN representation consisting of a uniform tensor O . (c) The tensor O is built by grouping the δ tensor with the connecting square root of the W matrix. The square root of the W tensor is obtained via singular value decomposition (SVD). The bond dimension of tensor O is labeled as d .

By grouping each δ tensor with the surrounding six square root of W matrix into a single tensor O , the partition function can be represented as a tensor network of uniform tensor O , as shown in Fig. 1(b)

$$\mathbb{Z} = \text{tTr} \prod_i O_i(s_1, s_2, s_3, s_4, s_5, s_6). \quad (5)$$

The partition function can further be reformulated as

$$\mathbb{Z} = \text{Tr} \{ \hat{T}(O)^{N_z} \} \quad (6)$$

where $\hat{T}(O)$ is the plane-to-plane transfer matrix composed of a plane of uniform local tensors O , and N_z is the number of sites in z-direction of the system.

In the thermodynamic limit, the central task is to solve for the leading eigenvalue and eigenvectors of the transfer matrix

$$\hat{T}(O) |\psi\rangle = \Lambda |\psi\rangle, \quad (7)$$

where the leading eigenvector $|\psi\rangle$ can be approximated by using an iPEPS, represented by a uniform tensor A with virtual bond dimension D . Eq. (7) can then be represented diagrammatically, as displayed in Fig. 2(a).

In the gradient-based optimization scheme, the eigen equation Eq. (7) is transformed into an optimization problem, aiming to minimize the cost function f with

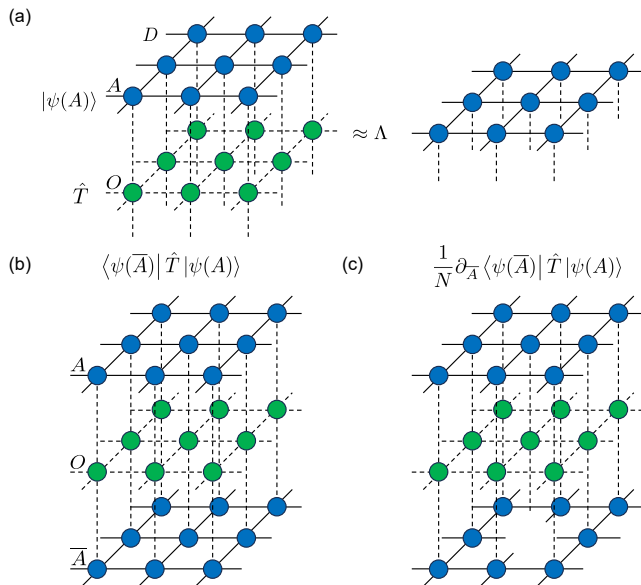


FIG. 2. iPEPS ansatz and the terms for calculating the free energy and gradient. (a) The fixed point equation for the transfer matrix. The iPEPS state $|\psi(A)\rangle$ and the plane-to-plane transfer matrix \hat{T} are made up of the uniform tensors A and O respectively. (b)-(c) Triple-layer network representations of the terms involved in the calculation of free energy and gradient.

respect to A

$$f(A, \bar{A}) = -\frac{1}{N\beta} \log(\Lambda) = -\frac{1}{N\beta} \log \left(\frac{\langle \psi(\bar{A}) | \hat{T} | \psi(A) \rangle}{\langle \psi(\bar{A}) | \psi(A) \rangle} \right), \quad (8)$$

where $N = N_x N_y$ is the number of sites in the xy-plane of the system and f has the physical meaning of the free energy density.

The gradient of the cost function is given by

$$g = 2 \times \partial_{\bar{A}} f(A, \bar{A}) = -\frac{2}{N\beta} \left(\frac{\partial_{\bar{A}} \langle \psi(\bar{A}) | \hat{T} | \psi(A) \rangle}{\langle \psi(\bar{A}) | \hat{T} | \psi(A) \rangle} - \frac{\partial_{\bar{A}} \langle \psi(\bar{A}) | \psi(A) \rangle}{\langle \psi(\bar{A}) | \psi(A) \rangle} \right). \quad (9)$$

Since both \hat{T} and $|\psi(A)\rangle$ are represented as tensor networks, the terms in the free energy density and the gradient can be represented as infinite $2D$ network, as shown in Fig. 2(b)-(c). By using approximate tensor network contraction method, one can compute the gradient and the value of the function with respect to A . Various optimization methods, such as the quasi-Newton method or conjugate-gradient method, can then be applied to iteratively solve for A .

A key bottleneck in this algorithm is the evaluation of the free energy and gradient, which involves contracting a triple-layer infinite tensor network at each optimization step. In the traditional reduced method, the contraction

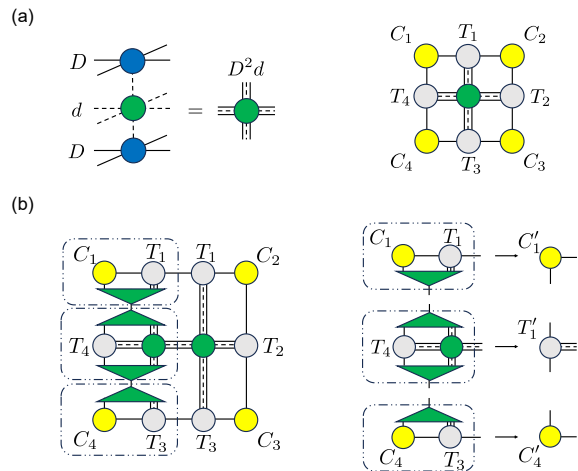


FIG. 3. Reduced CTMRG scheme for contracting the triple-layer network. (a) The environment tensor configuration for C and T . (b) The absorption and truncation procedure during a left move.

is first performed by contracting the physical indices connecting the different layers, resulting in a single-layer network, as shown in Fig. 3(a). The network can then be contracted by applying standard 2D tensor network contraction techniques. One commonly used technique is the CTMRG with directional moves [39–41], as illustrated in Fig. 3(b). In this approach, environment tensors, including corner tensors $\{C\}$ and edge tensors $\{T\}$, are used to approximate the environment after contracting the infinite network. The $\{C\}$ and $\{T\}$ tensors are solved using the power method. In each step, the system grows in one direction, and the local tensors from the system are absorbed into the environment tensors, which are subsequently truncated using projectors P .

For the triple-layer structure contracting by reduced method, the leading computation time of contraction is in the scale of [42]

$$\mathcal{O}(\chi^3 D^6 d^3) \sim \mathcal{O}(D^{12} d^3) \quad (10)$$

and the leading memory space cost is

$$\mathcal{O}(\chi^2 D^4 d^2) \sim \mathcal{O}(D^8 d^2). \quad (11)$$

The computation cost restricts the accessible bond dimension of iPEPS tensors in variational method. Previous work can only get reliable results with $D \leq 4$ for 3D classical Ising model [27, 28].

III. TRIPLE-LAYER SPLIT-CTMRG SCHEME

To reduce the computational cost associated with contracting a triple-layer tensor network, we propose a novel split-CTMRG method. Compared to the traditional reduced method, the split-CTMRG introduces two key dif-

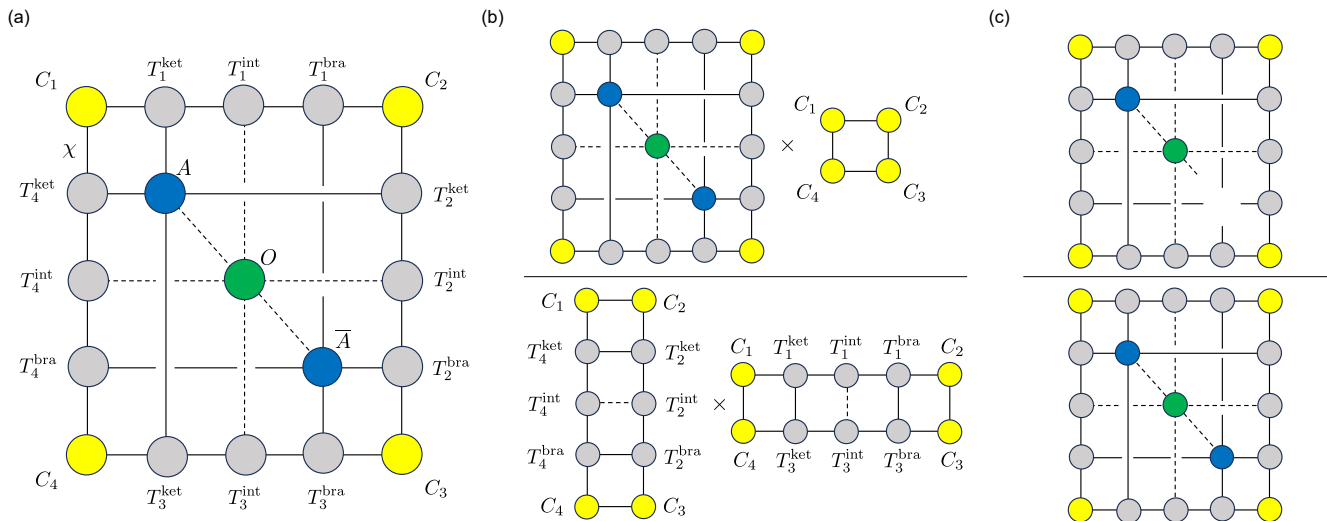


FIG. 4. The Split-CTM environment tensor setting. The bonds of the PEPO O are denoted by dashed lines, while the bonds of the PEPS and the environment are denoted by solid lines. (a) The Split-CTM environment tensor configuration for the triple-layer network. (b) The numerator term involved in calculating the free energy. (c) The term involved in calculating the gradient.

ferences. First, the local tensors with a triple-layer structure are compressed into a single-layer tensor network, where the physical indices are not contracted. Correspondingly, the environment edge tensors are decomposed into separate edge tensors for each layer. Second, while the local tensors corresponding to the original triple layers are absorbed in one move, the projectors are constructed and applied to the environment tensors in a separate, sequential manner. The details of the split-CTMRG method are presented below.

A. Environment tensor setting

As shown in Fig. 4(a), for a triple-layer tensor network, the environment tensors in the split-CTMRG scheme are set as $E = \{C_i, T_i^{\text{ket}}, T_i^{\text{int}}, T_i^{\text{bra}}, i = 1, 2, 3, 4\}$, where T_i^{ket} , T_i^{int} , and T_i^{bra} represent the edge tensors for each layer, and $\{C_i, i = 1, 2, 3, 4\}$ are the four corner matrices. In contrast to the original nested tensor network approach, which introduces swap tensors to transform the single-layer network into a regular multi-site network with regular lattice geometry (which is then contracted via a multi-site CTMRG scheme)[33], the split-CTMRG scheme directly projects the triple-layer network into a single-layer representation. In this representation, the local tensors O of the partition function are directly connected to the internal edge environment T^{int} . Furthermore, the structure of the environment tensors differs from that of the multi-site CTMRG method, where the number of corner and edge tensors scales as $4n_x n_y$, where $n_x \times n_y$ being the unit cell size. For a double-layer tensor network, the split-CTM environment is constructed in a similar manner as for the triple-layer case, with four corner tensors

and four edge tensors per layer, labeled as T^{ket} and T^{bra} .

Under this environment setup, both the free energy and gradient terms can be expressed in terms of the CTM tensors, as illustrated in Fig. 4(b)-(c). Here, we focus on the contraction of the triple-layer network and ignore the terms related to the normalization of $|\psi(A)\rangle$.

B. Renormalization scheme

For a general PEPO without any specific symmetry assumptions, the renormalization of the environment tensors is performed using directional moves. A complete split-CTMRG update consists of four directional moves: left, right, up, and down, which are applied sequentially until the environment converges. Here, we take the left move as an example to illustrate the CTMRG procedure, as shown in Fig. 5.

The main steps of the procedure are as follows.

1. As is shown in Fig. 5(a), insert a new set of tensors $\{T_1^{\text{ket}}, T_1^{\text{int}}, T_1^{\text{bra}}, T_3^{\text{ket}}, T_3^{\text{int}}, T_3^{\text{bra}}, A, O, \bar{A}\}$.
2. The newly inserted tensors in each row are contracted into the left environment tensors $\tilde{C}_1, \tilde{T}_4^{\text{ket}}, \tilde{T}_4^{\text{int}}, \tilde{T}_4^{\text{bra}}$, and \tilde{C}_4 (see Fig. 5(b)), resulting in the vertical bond dimension increasing.
3. In the split-CTM scheme, the isometric projectors are decomposed into multiple smaller projectors to reduce computational cost. Both the form and construction of the projectors have a certain degree of arbitrariness. The choice of whether to absorb and truncate the intermediate layer independently or in conjunction with the ket and bra layers leads to

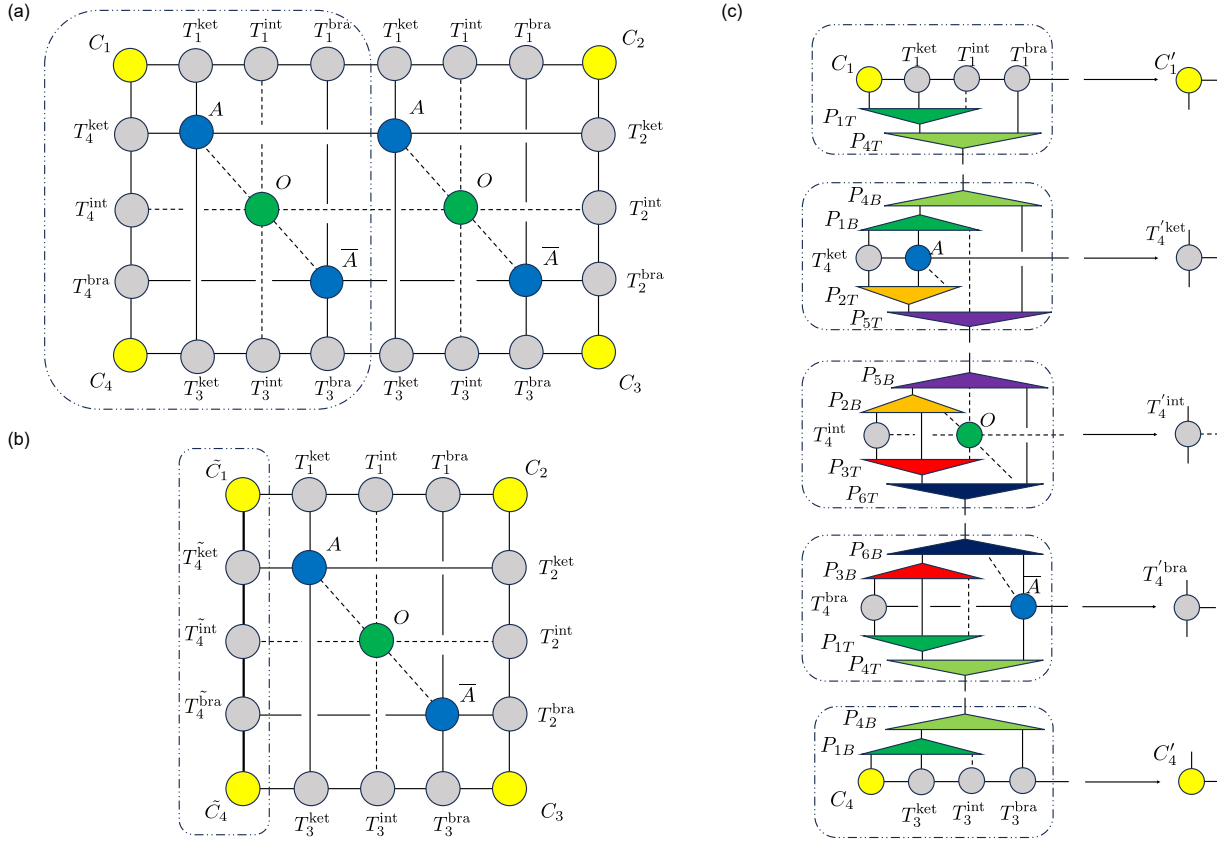


FIG. 5. Left move in the Split-CTMRG scheme for the triple-layer network. (a) Insertion. (b) Absorption. (c) Truncation.

different schemes. Here, we present a six-projector scheme in which the bonds of the PEPO tensor O are truncated alongside the projectors for the ket and bra layers. An alternative nine-projector scheme, in which the intermediate physical PEPO is absorbed and truncated independently, is discussed in section. V.

As illustrated in Fig. 5(c), isometric projectors $\{P_{aT}, P_{aB}, a = 1, 2, 3, 4, 5, 6\}$ are inserted along the vertical bonds to reduce the bond dimension. The isometry projectors with same index numbers are in the same group, satisfying the relation: $P_{aB}^\dagger P_{aT} = I$. For each vertical bond to be truncated, two projectors are used: one to truncate the bonds related with the ket layer and the other to truncate the bond related to the bra layer, This yields the updated environment tensors $C'_1, T_4^{\prime\text{ket}}, T_4^{\prime\text{int}}, T_4^{\prime\text{bra}}$, and C'_4 . The above procedure can be generalized to other directions straightforwardly.

In certain cases, lattice symmetries are preserved at the level of the transfer matrix and the local tensors. Exploiting these symmetries can further reduce the computational cost. For instance, in a cubic lattice, if the transfer matrix is real and symmetric, and the local PEPO tensor O is invariant under the O_h symmetry group, the PEPS tensor A can be chosen to be real, with its virtual bonds constrained to be invariant under the D_4 symme-

try group. Symmetry constraints can be imposed at each optimization step by projecting both the tensor A and its gradient g onto the symmetric subspace.

Moreover, in the split-CTMRG scheme, the nested structure reduces the symmetry from D_4 to D_2 , leading to the following constraints on the environment tensors

$$\begin{cases} C_1 = C_3, C_2 = C_4 \\ C_i = C_i^T, \quad i = 1, 2, 3, 4 \\ T_4^{\text{ket}} = (T_1^{\text{ket}})^T = T_2^{\text{bra}} = (T_3^{\text{bra}})^T \\ T_4^{\text{bra}} = (T_1^{\text{bra}})^T = T_2^{\text{ket}} = (T_3^{\text{ket}})^T \\ T_4^{\text{int}} = (T_1^{\text{int}})^T = T_2^{\text{int}} = (T_3^{\text{int}})^T \end{cases} \quad (12)$$

Here T_i^T means the transpose operation on the virtual bonds of edge tensors. With these symmetry constraints, a symmetric split-CTMRG scheme becomes more efficient than the directional move scheme, since all corner and edge tensors can be updated using a single set of projectors. While the edge tensors are renormalized in the same manner as in the directional scheme, the absorption and truncation of corner tensors is done in a different way, as illustrated in Fig. 7.

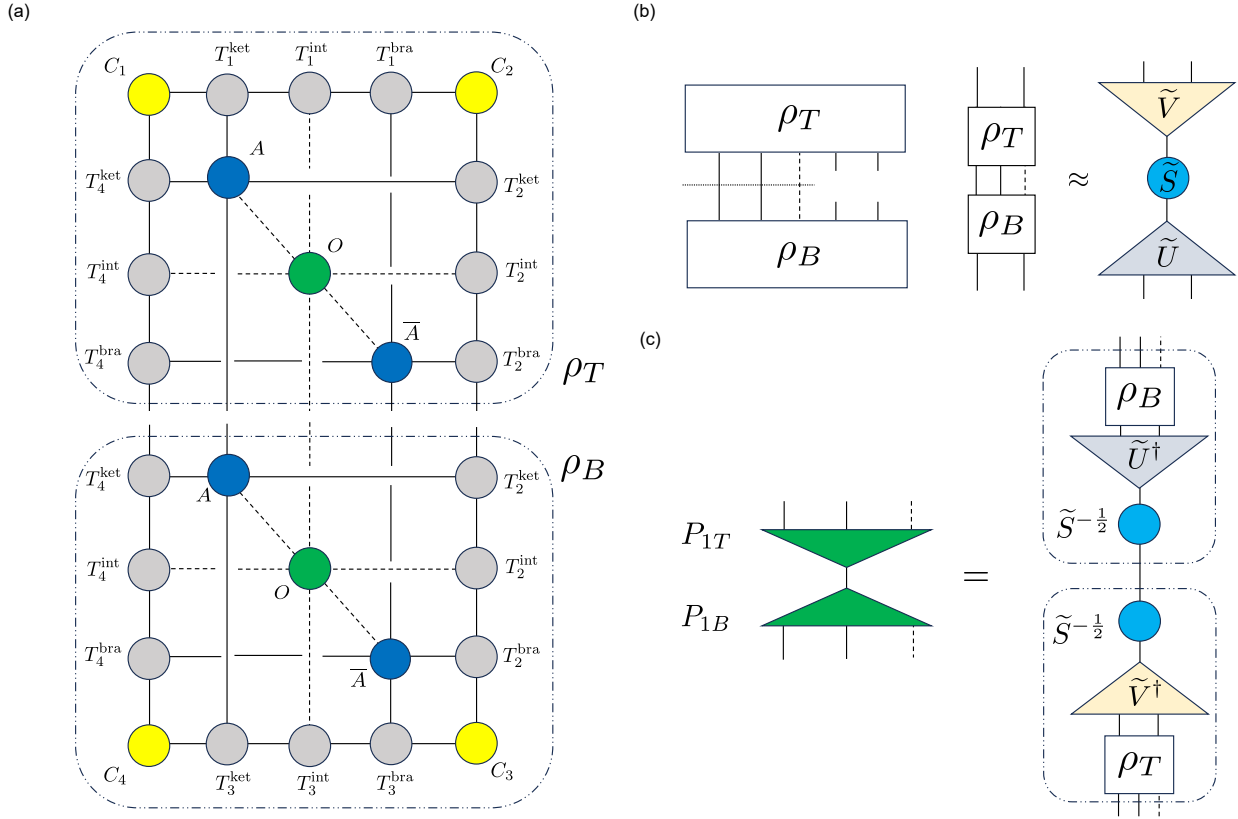


FIG. 6. Construction of projector 1. (a) ρ_T and ρ_B consist of patches of tensors representing the top and bottom environments. (b) SVD is performed on $\rho_B \rho_T$, yielding $\tilde{U}, \tilde{S}, \tilde{V}$. The largest χ singular values is keeping. (c) A pair of projectors are constructed to approximate isometry.

C. Projectors construction

Projectors serve as approximate isometries inserted between the bonds to be truncated. The construction scheme is generally not unique. Here we apply the commonly used method developed in Ref. [41]. As depicted in Fig. 6(a), we consider an effective environment consisting of 1×2 unit cells of the local tensor set $\{A, O, \bar{A}\}$ along with the surrounding environment tensors to build the projector. The environment is further divided into two parts: one corresponding to the upper-half environment ρ_T and the other to the lower-half environment ρ_B . The dangling indices of ρ_T and ρ_B are then regrouped into two sets: one set contains the indices to be truncated, while the other index contains the remaining indices. Thus ρ_T and ρ_B can be treated as matrix.

As illustrated in Fig. 6(b)-(c), the projectors can be built by using the following identity

$$I = \rho_T \rho_T^{-1} \rho_B^{-1} \rho_B = \rho_T (\rho_B \rho_T)^{-1} \rho_B = \rho_T \tilde{V}^\dagger \tilde{S}^{-1} \tilde{U}^\dagger \rho_B, \quad (13)$$

where I represent the identity operator, and $\tilde{U}, \tilde{S}, \tilde{V}$ are the matrices obtained through the singular value decom-

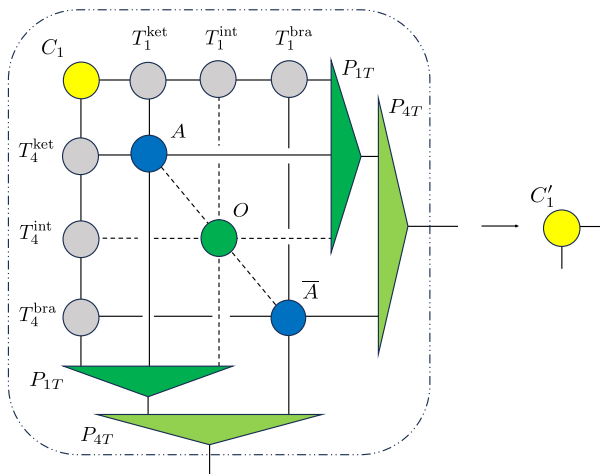


FIG. 7. Symmetric absorption and truncation of corner tensors in the triple-layer split-CTMRG scheme.

position of the matrix $\rho_E = \rho_B \rho_T$, as follows:

$$\rho_B \rho_T = \tilde{U} \tilde{S} \tilde{V}. \quad (14)$$

By splitting and truncating the singular spectrum of S , the projectors P_{1T} and P_{1B} are obtained

$$P_{1T} = \rho_T \tilde{V}^\dagger \tilde{S}^{-\frac{1}{2}}, \quad P_{1B} = \tilde{S}^{-\frac{1}{2}} \tilde{U}^\dagger \rho_B. \quad (15)$$

The other five projectors used in Fig. 5 can be calculated in a similar manner to P_{1T}, P_{1B} but with different choices of the effective environment ρ_T and ρ_B . While the detailed construction of each projectors are presented in the appendix, we briefly discuss the general principle for selecting ρ_T and ρ_B .

There is a trade-off between efficiency and accuracy when choosing ρ_T and ρ_B . While using larger tensors for ρ_T and ρ_B may improve accuracy by capturing more relevant basis, it can also increase the computational cost. We observe that $\rho_B \rho_T$ can be viewed as a successive product of four matrices at the corner (connected by the virtual bonds) and the number of non-zero singular values is bounded by the smallest rank of these matrices. Hence, we also make sure that the bond dimensions of the four corners are larger than the bond dimensions to be truncated to.

The leading computation cost of the entire scheme arises during the construction of projector 4, which can be reduced to a scale of

$$\mathcal{O}(\chi^3 D^3 d^3) \sim \mathcal{O}(D^9 d^3). \quad (16)$$

while the memory cost is reduced to

$$\mathcal{O}(\chi^2 D^3 d^2) \sim \mathcal{O}(D^7 d^2). \quad (17)$$

D. Convergence criterion

The singular value spectrum of the effective density matrix formed by the four corner tensors is used to check the convergence of the algorithm. The effective density matrix ρ_{eff} is given by:

$$\rho_{\text{eff}} = \frac{C_1 C_2 C_3 C_4}{\text{Tr}(C_1 C_2 C_3 C_4)} = U S V^T, \quad (18)$$

where ρ_{eff} represents the effective density matrix of the system, and S is the diagonalized matrix containing the singular-values from the decomposition.

Convergence is determined by monitoring the change in the singular value spectrum between two successive steps. If the difference between the spectra is below a specified threshold, the CTMRG procedure is considered to have converged

$$\|S^{[i+1]} - S^{[i]}\|_2 < \delta, \quad (19)$$

where $\|\cdot\|_2$ denotes the l_2 -norm.

IV. BENCHMARK: 3D ISING MODEL

We apply our method to the 3D classical Ising model on a cubic lattice as a benchmark. The Hamiltonian of the Ising model in the absence of an external field is given by

$$H = - \sum_{\langle i,j \rangle} \sigma_i \sigma_j, \quad (20)$$

where $\sigma_i = \pm 1$. The Boltzmann weight on each links is represented as

$$W = \begin{pmatrix} e^\beta & e^{-\beta} \\ e^{-\beta} & e^\beta \end{pmatrix}, \quad (21)$$

where β is the inverse temperature. The PEPO for the Ising model can be constructed using Eq.(4) and Eq.(5). In this case, the local PEPO tensor respects the full cubic point group symmetry O_h , and we apply the symmetric split-CTMRG method for iPEPS optimization of the 3D Ising model.

A. Accuracy and efficiency

Before discussing the physical results, we first demonstrate that the free energy density and the gradient of the system can be calculated accurately, with a significant speed-up achieved using the split-CTMRG scheme. This speed-up without losing accuracy is crucial for enabling the use of larger bond dimensions for the tensor A in gradient-based optimization.

We contract the double-layer and triple-layer network for an Ising PEPO tensor O at a certain temperature and an optimized iPEPS tensor A , using both the reduced and split CTMRG methods to calculate free energy and gradient. As shown in Fig. 8(a) and (b), the split method could yields results comparable to the reduced method though a larger χ is required to reach the same accuracy.

Compared to the reduced method, the split method has a lower leading computation cost, though it comes with a larger prefactor that scales linearly with the number of projectors. In our tests, the split method becomes more efficient than the reduced method when the bond dimension exceeds $D = 5$, with the advantage becoming more pronounced as the bond dimension increases, as shown in Fig. 8 (c).

When applied to gradient-based variational optimization, the split method also shows an obvious speedup. In the cases tested, optimization using the split method requires approximately the same number of steps to converge to the same accuracy as the reduced method, as shown in Fig. 8(d). Therefore, the speedup for optimization is similar to that for each step of CTMRG convergence.

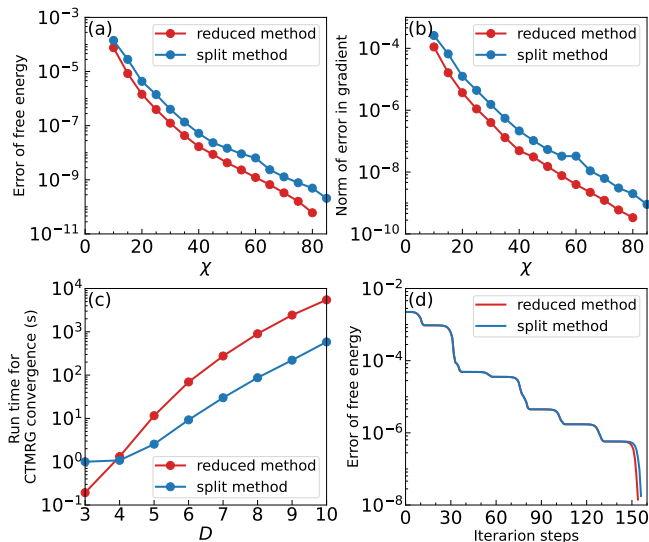


FIG. 8. Benchmark of accuracy and efficiency for the Split-CTMRG scheme. (a),(b) Comparison of the error in free energy and the norm of the error in gradient for two methods at different bond dimensions χ . Data points are taken at $T = 4.4$ with $D = 6$. (c) Runtime for CTMRG convergence. The contraction is performed with a converged A at $T=4.4$ for various D values, with $\chi = D^2$. The convergence criterion is taken to be $\delta = 10^{-10}$. (d) Error in free energy for the two methods during optimization at $T=4.4$. The error is calculated relative to the converged result of the reduced method.

B. Physical quantities

This section presents the results of thermal quantities calculated using the split-CTMRG scheme. The optimization of the iPEPS tensor A was performed via a L-BFGS method, with the convergence criterion was set to $\|g\|_\infty < 10^{-7}$. Physical quantities were subsequently computed using the split-CTM environment, in which the local Ising PEPO tensor is replaced by the corresponding impurity tensor.

The temperature dependence of magnetization M obtained using both the reduced method and the split method, in comparison with the Monte Carlo result[1, 2], is shown in Fig. 9(a). The results from the split method with same bond dimension ($D = 3, \chi = 60$) exhibit excellent agreement with those from the reduced method. In the off-critical regions, the magnetization obtained through the split method with different bond dimensions is consistent with the Monte Carlo result. While in the critical region, as the bond dimension increases ($D = 3 - 6, \chi = 60 - 100$), the magnetization curve converge towards the Monte Carlo results. From the singular point of the magnetization curve, the critical temperature is estimated to be $T_c = 4.51288(13)$, which is comparable with the Monte Carlo result [3, 43] $T_c = 4.511523$ and the high-order tensor renormalization group (HOTRG) result [12] $T_c = 4.511544$.

Furthermore, as shown in Fig. 9(b), by fitting the nu-

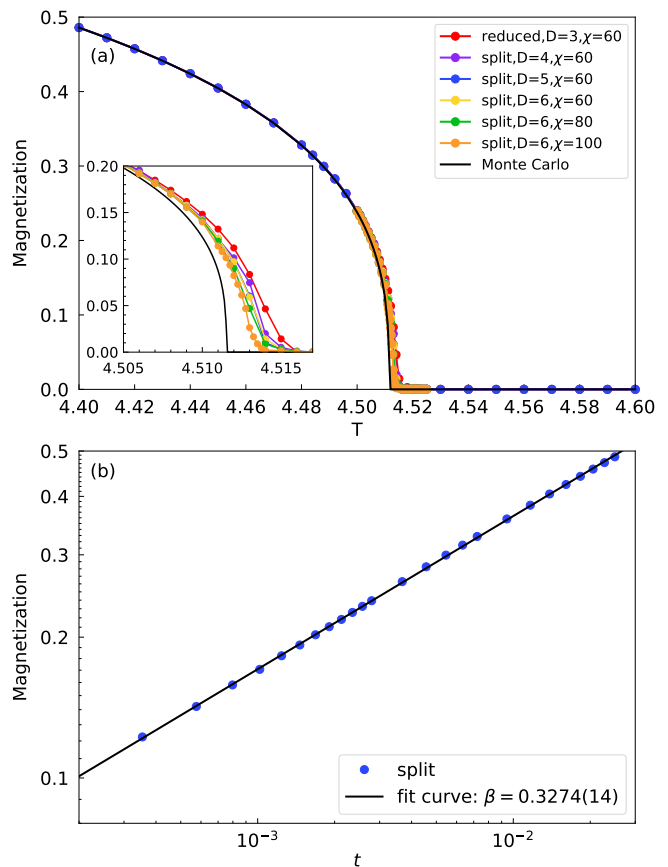


FIG. 9. (a) Magnetization for the 3D Ising model as a function of temperature, computed using different methods and bond dimension. Inset: Magnetization curve in the critical region. (b) Fit of the critical exponent β . Magnetization data from $T=4.4$ to $T=4.511$ are used for the fit.

merical data of M in the near-critical region with the formula:

$$M \sim t^\beta, \quad (22)$$

where $t = \frac{|T-T_c|}{T_c}$, we obtain the critical exponent $\beta = 0.3274(14)$, which is consistent with the previous Monte Carlo result [3] $\beta = 0.3263$ and the HOTRG result [12] $\beta = 0.3295$.

The temperature dependence of the internal energy U and specific heat C_v are shown in Fig. 10, where C_v is obtained by taking the numerical derivative of the $U(T)$. These two quantities also agree well with the Monte Carlo results over a wide temperature range, with slight deviations near the critical point. From the peak of heat capacity, the critical temperature is estimated as $T_c = 4.5120(5)$, which is consistent with the value obtained from the magnetization curve. These results indicate that the split-CTMRG works well in the 3D classical model.

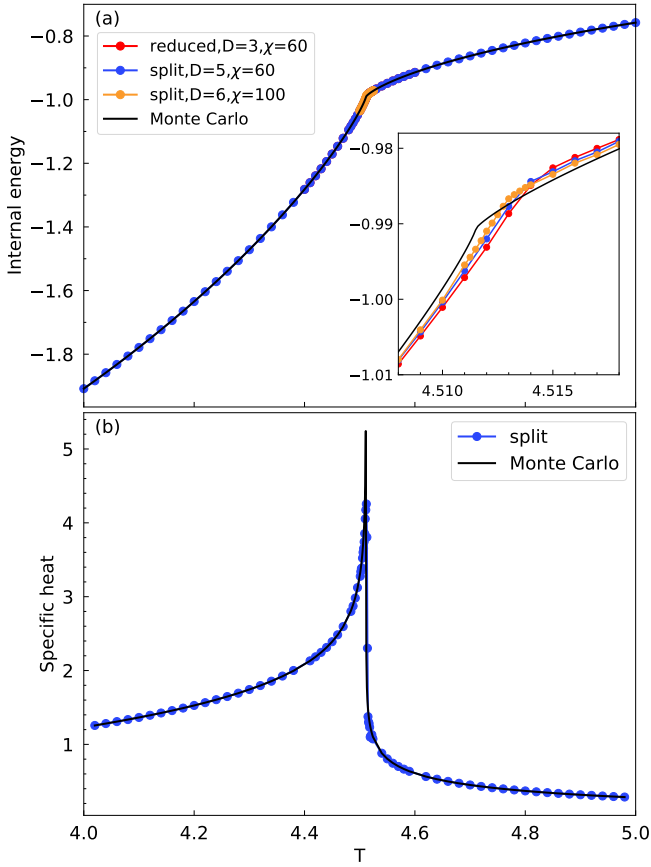


FIG. 10. (a) Internal energy and (b) specific heat for the 3D Ising model as a function of temperature, computed using different methods and bond dimension.

V. DISCUSSION AND OUTLOOK

In this paper, we introduce a split-CTMRG scheme designed to accelerate the variational optimization of three-dimensional statistical models. The proposed method achieves a reduced leading computational cost of $O(D^9)$, demonstrating a clear efficiency advantage over the traditional reduced method for the 3D classical Ising model when $D \geq 5$. Using this approach, we obtain iPEPS tensors with high bond dimensions (e.g., ($D = 6$)), and the physical results are in agreement with the state-of-the-art Monte Carlo and tensor network calculations.

Looking ahead, several promising directions can be explored to further develop and apply the algorithm. While this work focuses on the split-CTM scheme for single-site PEPOs, its generalization to multi-site PEPOs is straight forward. Additionally, to further enhance computational efficiency, the iterative application of projectors to environment tensors may be replaced by directly solving fixed-point equations, as discussed in Ref. [44, 45].

Although our primary focus has been on variational optimization for 3D classical systems, the method is also applicable to 2D quantum systems, where the Hamiltonian can be represented as a PEPO. Furthermore, for

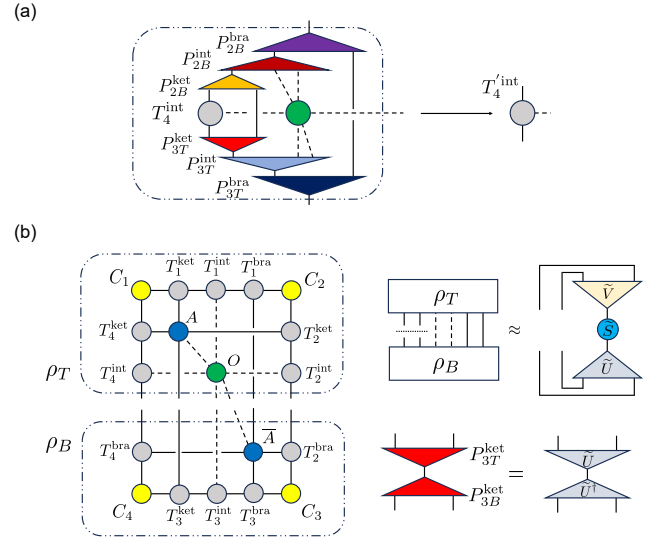


FIG. 11. Nine-projector scheme. (a) The absorption and truncation of T_4^{int} in the nine-projector scheme. (b) The construction of projector P_{3T}^{ket} in the nine-projector scheme.

spin systems beyond the Ising spin, it may be necessary to treat PEPOs with bond dimensions comparable to those of PEPS. In such cases, the bonds of the PEPOs can be truncated using separate projectors, which leads to an alternative nine-projector scheme. As illustrated in Fig. 11(a), for the renormalization of edge tensors T_4^{int} , three projectors $\{P_i^{\text{ket}}, P_i^{\text{int}}, P_i^{\text{bra}}\}$ are inserted between the vertical bonds, where the vertical bonds of the PEPO tensor O are truncated by P_i^{int} . Since in this scheme the number of bonds truncated by each projector is fewer than the six-projector scheme, the construction of projectors as described in subsection III C, where the singular value decomposition (SVD) is applied to the non-truncated indices of the effective environment, is no longer computationally efficient. For instance, as shown in Fig. 11(b), when an effective environment including a 1×1 unit cell of the local tensor set $\{A, O, \bar{A}\}$ is used to build the projectors $\{P_{3T}^{\text{ket}}, P_{3B}^{\text{ket}}\}$, the computational cost of the SVD as given by Eq.(14) scales as $\mathcal{O}(\chi^3 D^3 d^6)$. Instead, one can employ the method proposed in Ref.[40], where the SVD is applied to the bonds to be truncated (see Fig. 11(b)). This would reduce the computational cost to $\mathcal{O}(\chi^3 D^3)$.

The consideration discussed above is also relevant for generalizing the algorithms to multi-layer PEPOs, such as those encountered in classical frustrated spin systems in 3D or 2D models with multi-layer structures (e.g., multi-layer or multi-band superconducting systems). These extensions will be tested in future work.

Acknowledgments. The authors are very grateful to Zhi-Yuan Xie and Shuo Yang for stimulating discussions. The research is supported by the National Key Research and Development Program of China (Grant No. 2023YFA1406400).

Appendix: Construction of the projectors

1. Six-projector scheme

In the main text, we utilize a six-projector scheme, where the legs of the PEPO tensor O are truncated using projectors for the ket and bra layers. The construction of projectors 1 is illustrated in Fig. 6, and the construction of the remaining projectors is detailed below. Since all the projectors are constructed using Eq.(14) and Eq.(15), we only provide a description of the effective environments ρ_T and ρ_B for each projector. For large effective environment, such as those shown in Fig. 14, the optimal contraction order varies with the choices of d, D, χ and cannot be directly determined. Therefore, the computational cost of tensor contraction listed below and in the main text is determined numerically, assuming $d \ll D$, with $\chi \sim D^2$, which serves as an upper bound on the computational cost of contraction.

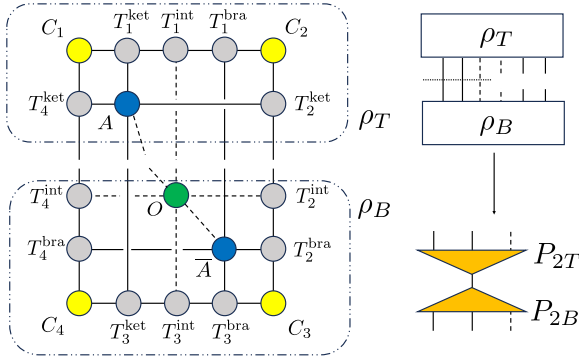


FIG. 12. The construction of projector 2.

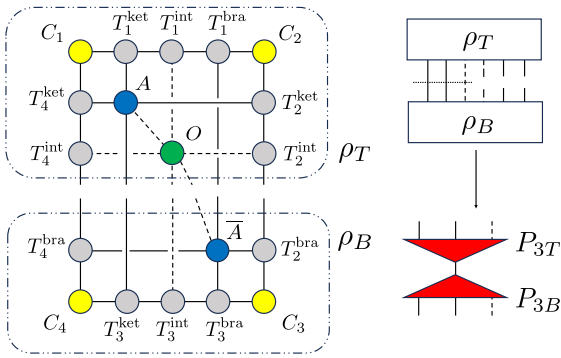


FIG. 13. The construction of projector 3.

The construction of projector 2 and 3 is shown in Fig. 12 and Fig. 13. The effective environment is cho-

sen to consist of a 1×1 unit-cell of the local tensor set $\{A, O, \bar{A}\}$, along with the surrounding environment tensors. These projectors truncate the bond dimension from $\chi D d$ to χ . The leading computation cost arises from tensor contraction and SVD, with a scale of

$$\mathcal{O}(\chi^3 D^3 d^3). \quad (\text{A.1})$$

The construction of projectors 4, 5 and 6 leverages projectors 1, 2 and 3 to reduce the cost associated with SVD decompositions and tensor contraction. For projector 4, two constructions are considered. The full projector 4 as shown in Fig. 14 (a) is built based on an effective environment consisting of 2×2 unit-cells of the local tensor set $\{A, O, \bar{A}\}$, with the surrounding environment and local tensors from bra layer already renormalized by P_{1T} and P_{1B} . while the half projector 4, as shown in Fig. 14 (b), uses a 2×1 unit-cells of the local tensor set $\{A, O, \bar{A}\}$, with the surrounding environment and local tensors from the bra layer renormalized by P_{1T}, P_{1B} and P_{1L}^U, P_{1L}^D . Here P_{1L}^U and P_{1L}^D represent the projectors 1 calculated during the up move and down move, respectively.

For the full projector 4, the leading computation cost arises from tensor contractions, with a scale of

$$\mathcal{O}(\chi^3 D^4 d). \quad (\text{A.2})$$

For the half projector 4, the computation cost is reduced to

$$\mathcal{O}(\chi^3 D^3 d^3) \sim \mathcal{O}(D^9 d^3). \quad (\text{A.3})$$

Although half projectors are regarded as less accurate than full projectors in some situations [36, 41], we don't observe accuracy issues compared to the full projectors in our numerical benchmarks. Therefore, in the main text, we use the computational cheaper half projectors.

Projectors 5 and 6 are built by considering an effective environment consisting of 1×2 unit-cells of the local tensor set $\{A, O, \bar{A}\}$, with the surrounding environment and local tensors from the bra layer already renormalized by $\{P_{2T}, P_{2B}, P_{2T}^R\}, P_{2B}^R$ and $\{P_{3T}, P_{3B}, P_{3T}^R, P_{3B}^R\}$, respectively. Here P_2^R, P_3^R represent the projectors 2, 3 calculated during the right move.

The leading computational cost for these projectors also arises from tensor contractions as well as SVD, with a scale of

$$\mathcal{O}(\chi^3 D^3 d^3). \quad (\text{A.4})$$

The overall leading computational cost of the entire scheme is therefore

$$\mathcal{O}(\chi^3 D^3 d^3) \sim \mathcal{O}(D^9 d^3). \quad (\text{A.5})$$

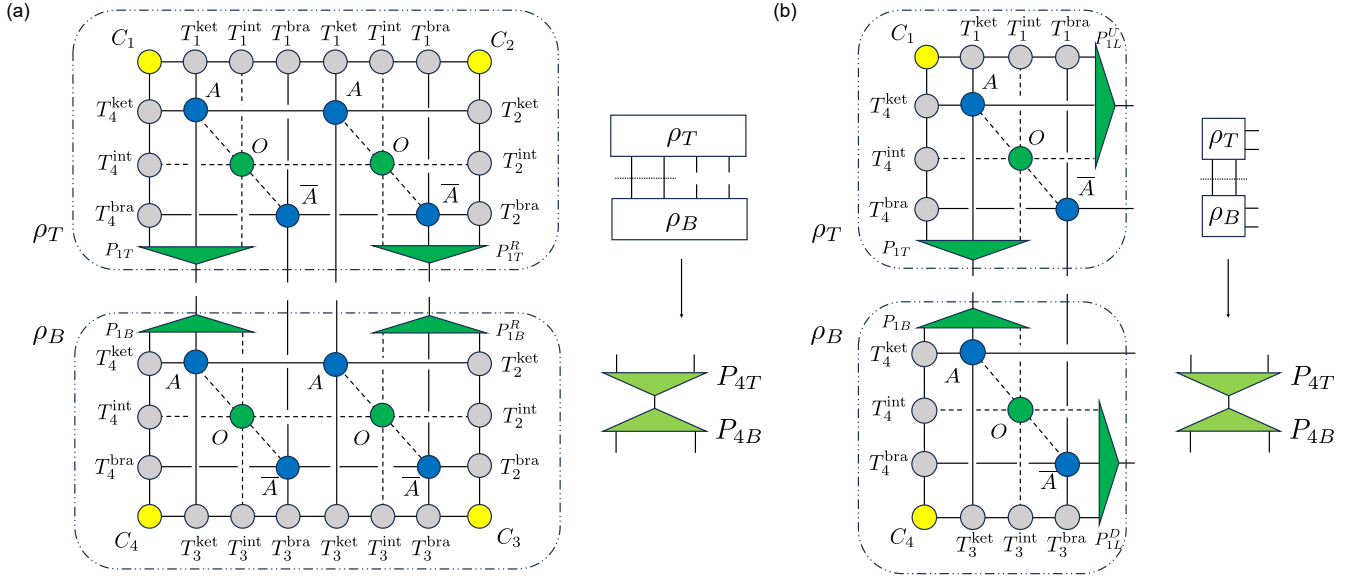


FIG. 14. The construction of projector 4. (a) Full projector construction. P_{1T}^R and P_{1B}^R are the projectors calculated in the right move. In the D_2 symmetric split-CTMRG scheme, $P_{1T}^R = P_{1B}$, $P_{1B}^R = P_{1T}$. (b) Half projector construction. P_{1L}^U and P_{1L}^D are the projectors calculated in the up and down move. In the D_2 symmetric split-CTMRG scheme, $P_{1L}^U = (P_{1T})^T$, $P_{1L}^D = (P_{1B})^T$.

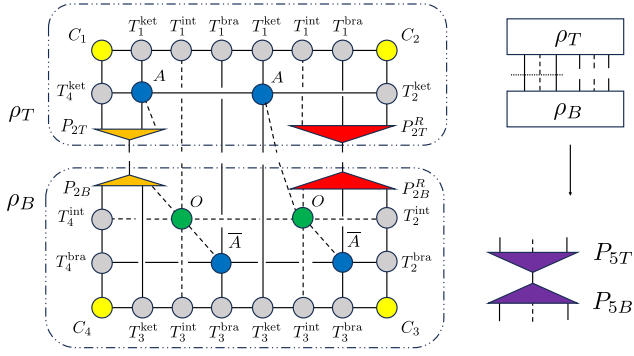


FIG. 15. The construction of projector 5. P_{2T}^R and P_{2B}^R are the projectors calculated in the right move. In the D_2 symmetric split-CTMRG scheme, $P_{2T}^R = P_{3B}$, $P_{2B}^R = P_{3T}$.

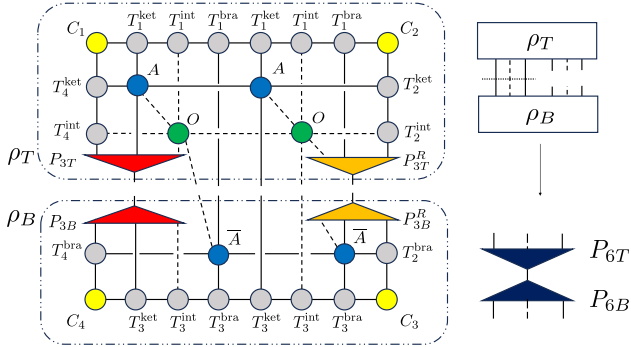


FIG. 16. The construction of projector 6. P_{3T}^R and P_{3B}^R are the projectors calculated in the right move. In the D_2 symmetric split-CTMRG scheme, $P_{3T}^R = P_{2B}$, $P_{3B}^R = P_{2T}$.

- [1] A. L. Talapov and H. W. J. Blöte, The magnetization of the 3D Ising model, *Journal of Physics A: Mathematical and General* **29**, 5727 (1996).
- [2] X. Feng and H. W. J. Blöte, Specific heat of the simple-cubic Ising model, *Physical Review E* **81**, 031103 (2010).
- [3] A. M. Ferrenberg, J. Xu, and D. P. Landau, Pushing the limits of Monte Carlo simulations for the three-dimensional Ising model, *Physical Review E* **97**, 043301 (2018).
- [4] S. El-Showk, M. F. Paulos, D. Poland, S. Rychkov, D. Simmons-Duffin, and A. Vichi, Solving the 3D Ising model with the conformal bootstrap, *Physical Review D* **86**, 025022 (2012).
- [5] S. El-Showk, M. F. Paulos, D. Poland, S. Rychkov, D. Simmons-Duffin, and A. Vichi, Solving the 3d Ising Model with the conformal bootstrap ii. c -minimization and precise critical exponents, *Journal of Statistical Physics* **157**, 869 (2014).
- [6] F. Kos, D. Poland, D. Simmons-Duffin, and A. Vichi, Precision islands in the Ising and $O(N)$ models, *Journal of High Energy Physics* **2016**, 36 (2016).
- [7] G. Vidal, Classical Simulation of Infinite-Size Quantum Lattice Systems in One Spatial Dimension, *Physical Review Letters* **98**, 070201 (2007).
- [8] R. Orus and G. Vidal, The iTEDB algorithm beyond unitary evolution, *Physical Review B* **78**, 155117 (2008), arXiv:0711.3960.
- [9] M. Levin and C. P. Nave, Tensor renormalization group approach to two-dimensional classical lattice models, *Physical Review Letters* **99**, 120601 (2007).
- [10] H. H. Zhao, Z. Y. Xie, Q. N. Chen, Z. C. Wei, J. W. Cai, and T. Xiang, Renormalization of tensor-network states, *Physical Review B* **81**, 174411 (2010).
- [11] Z. Y. Xie, H. C. Jiang, Q. N. Chen, Z. Y. Weng, and T. Xiang, Second renormalization of tensor-network states, *Physical Review Letters* **103**, 160601 (2009).
- [12] Z. Y. Xie, J. Chen, M. P. Qin, J. W. Zhu, L. P. Yang, and T. Xiang, Coarse-graining renormalization by higher-order singular value decomposition, *Physical Review B* **86**, 045139 (2012).
- [13] T. Nishino and K. Okunishi, Corner transfer matrix renormalization group method, *Journal of the Physical Society of Japan* **65**, 891 (1996), arXiv:cond-mat/9507087.
- [14] J. Haegeman and F. Verstraete, Diagonalizing transfer matrices and matrix product operators: A medley of exact and computational methods, *Annual Review of Condensed Matter Physics* **8**, 355 (2017).
- [15] V. Zauner-Stauber, L. Vanderstraeten, M. T. Fishman, F. Verstraete, and J. Haegeman, Variational optimization algorithms for uniform matrix product states, *Physical Review B* **97**, 045145 (2018).
- [16] L. Vanderstraeten, J. Haegeman, and F. Verstraete, Tangent-space methods for uniform matrix product states, *SciPost Physics Lecture Notes*, 7 (2019).
- [17] L. Vanderstraeten, B. Vanhecke, A. M. Laeuchli, and F. Verstraete, Approaching the Kosterlitz-Thouless transition for the classical XY model with tensor networks, *Physical Review E* **100**, 062136 (2019), arXiv:1907.04576.
- [18] Z.-Q. Li, L.-P. Yang, Z. Y. Xie, H.-H. Tu, H.-J. Liao, and T. Xiang, Critical properties of the two-dimensional q -state clock model, *Phys. Rev. E* **101**, 060105 (2020).
- [19] P. Scholl, A. Kshetrimayum, J. Eisert, R. Orus, and M. Rizzi, The classical two-dimensional Heisenberg model revisited: An $SU(2)$ -symmetric tensor network study, *SciPost Physics* **11**, 098 (2021), arXiv:2106.06310.
- [20] B. Vanhecke, J. Colbois, L. Vanderstraeten, F. Verstraete, and F. Mila, Solving frustrated Ising models using tensor networks, *Physical Review Research* **3**, 013041 (2021).
- [21] J. Colbois, B. Vanhecke, L. Vanderstraeten, A. Smerald, F. Verstraete, and F. Mila, Partial lifting of degeneracy in the $J_1-J_2-J_3$ Ising antiferromagnet on the Kagome lattice, *Physical Review B* **106**, 174403 (2022).
- [22] F.-F. Song, T.-Y. Lin, and G.-M. Zhang, General tensor network theory for frustrated classical spin models in two dimensions, *Physical Review B* **108**, 224404 (2023).
- [23] T. Nishino, K. Okunishi, Y. Hieida, N. Maeshima, and Y. Akutsu, Self-consistent tensor product variational approximation for 3D classical models, *Nuclear Physics B* **575**, 504 (2000).
- [24] T. Nishino, Y. Hieida, K. Okunishi, N. Maeshima, Y. Akutsu, and A. Gendiar, Two-dimensional tensor product variational formulation, *Progress of Theoretical Physics* **105**, 409 (2001).
- [25] K. Okunishi and T. Nishino, Kramers-Wannier approximation for the 3D Ising model, *Progress of Theoretical Physics* **103**, 541 (2000).
- [26] N. Maeshima, Y. Hieida, Y. Akutsu, T. Nishino, and K. Okunishi, Vertical density matrix algorithm: A higher-dimensional numerical renormalization scheme based on the tensor product state ansatz, *Physical Review E* **64**, 016705 (2001).
- [27] L. Vanderstraeten, B. Vanhecke, and F. Verstraete, Residual entropies for three-dimensional frustrated spin systems with tensor networks, *Physical Review E* **98**, 042145 (2018).
- [28] B. Vanhecke, J. Hasik, F. Verstraete, and L. Vanderstraeten, Scaling Hypothesis for Projected Entangled-Pair States, *Physical Review Letters* **129**, 200601 (2022).
- [29] T. Nishino and K. Okunishi, A density matrix algorithm for 3D classical models, *Journal of the Physical Society of Japan* **67**, 3066 (1998).
- [30] R. Orús, Exploring corner transfer matrices and corner tensors for the classical simulation of quantum lattice systems, *Physical Review B* **85**, 205117 (2012).
- [31] D. Adachi, T. Okubo, and S. Todo, Anisotropic tensor renormalization group, *Physical Review B* **102**, 054432 (2020), arXiv:1906.02007.
- [32] Y. Zhang, Q. Yang, and P. Corboz, Accelerating two-dimensional tensor network contractions using QR-decompositions (2025), arXiv:2505.00494.
- [33] Z. Y. Xie, H. J. Liao, R. Z. Huang, H. D. Xie, J. Chen, Z. Y. Liu, and T. Xiang, Optimized contraction scheme for tensor-network states, *Physical Review B* **96**, 045128 (2017).
- [34] L.-P. Yang, Y. F. Fu, Z. Y. Xie, and T. Xiang, Efficient calculation of three-dimensional tensor networks, *Physical Review B* **107**, 165127 (2023).
- [35] W. Lan and G. Evenbly, Reduced Contraction Costs of Corner-Transfer Methods for PEPS (2023),

- arXiv:2306.08212.
- [36] J. Naumann, E. L. Weerdenburg, J. Eisert, M. Rizzi, and P. Scholl, Variationally optimizing infinite projected entangled-pair states at large bond dimensions: A split corner transfer matrix renormalization group approach, *Physical Review B* **111**, 235116 (2025).
- [37] P. Corboz, Variational optimization with infinite projected entangled-pair states, *Physical Review B* **94**, 035133 (2016).
- [38] L. Vanderstraeten, J. Haegeman, P. Corboz, and F. Verstraete, Gradient methods for variational optimization of projected entangled-pair states, *Physical Review B* **94**, 155123 (2016).
- [39] R. Orus and G. Vidal, Simulation of two dimensional quantum systems on an infinite lattice revisited: Corner transfer matrix for tensor contraction, *Physical Review B* **80**, 094403 (2009), arXiv:0905.3225.
- [40] P. Corboz, S. R. White, G. Vidal, and M. Troyer, Stripes in the two-dimensional $t - J$ model with infinite projected entangled-pair states, *Physical Review B* **84**, 041108 (2011).
- [41] P. Corboz, T. M. Rice, and M. Troyer, Competing states in the t - J model: Uniform d -wave state versus stripe state, *Physical Review Letters* **113**, 046402 (2014).
- [42] The complexity analysis in this article is taken under the assumptions that d are relatively small compared with D and empirically χ should be at least the order of D^2 .
- [43] M. Hasenbusch, Finite size scaling study of lattice models in the three-dimensional ising universality class, *Phys. Rev. B* **82**, 174433 (2010).
- [44] M. T. Fishman, L. Vanderstraeten, V. Zauner-Stauber, J. Haegeman, and F. Verstraete, Faster methods for contracting infinite two-dimensional tensor networks, *Physical Review B* **98**, 235148 (2018).
- [45] X. F. Liu, Y. F. Fu, W. Q. Yu, J. F. Yu, and Z. Y. Xie, Variational corner transfer matrix renormalization group method for classical statistical models, *Chinese Physics Letters* **39**, 067502 (2022), arXiv:2203.17098.